

# Non-equilibrium wall model for large eddy simulations of complex flows exhibiting turbulent smooth body separation

Rahul Agrawal\*

*Center for Turbulence Research, Stanford University,*

Sanjeeb T. Bose

*Cadence Design Systems, Inc. and  
Institute for Computational and Mathematical Engineering, Stanford University,*

Parviz Moin

*Center for Turbulence Research, Stanford University.*

(Dated: July 17, 2024)

In this work, a non-equilibrium wall model is proposed for the prediction of turbulent flows experiencing adverse pressure gradients, including separated flow regimes. The mean-flow non-equilibrium is identified by comparing two characteristic velocities: the friction velocity ( $u_\tau$ ) and the viscous-pressure gradient velocity ( $u_p$ ). In regions where the pressure gradient velocity is comparable to the friction velocity ( $u_p \sim u_\tau$ ), the near-wall turbulent closure is modified to include the effect of the pressure-gradient and convective terms. The performance of this wall model is evaluated in two canonical flows experiencing smooth body separation: the NASA/Boeing speed bump and the Bachalo-Johnson bump. Improvements in the predictive capabilities of the proposed model for the conventional equilibrium wall model are theorized and then demonstrated through numerical experiments. In particular, the proposed wall model is able to capture the onset of boundary layer separation observed in experiments or DNS calculations at resolutions where the equilibrium wall model fails to separate.

## I. INTRODUCTION

As the Reynolds number of a wall-bounded flow increases, the feasibility of direct numerical simulations (DNS) becomes impractical due to an increasing separation between the large, energetic scales of motion and the small, dissipative scales [1]. The large-eddy simulation (LES) paradigm is an approach in which the larger scales of motion of the flow are explicitly evaluated, while the effect of the unresolved scales on larger eddies is modeled using a “subgrid-stress closure”. Several models have been proposed, including both phenomenological models [2–7] and data-driven methods [8, 9]. These approaches have been widely successful in predicting the correct turbulence statistics in canonical flows such as homogeneous isotropic turbulence [4], turbulent channels [10], and boundary layers [11]. At low or moderate Reynolds numbers, it is computationally feasible for LES resolutions to resolve near-wall viscous length scales, and as a result, no-slip boundary conditions can be applied due to accurate estimates of the near-wall velocity gradients. This is often referred to as a wall-resolved LES regime.

For many engineering flows of interest, even wall-resolved large-eddy simulations are impractical since the grid-point scaling of wall-resolving LES is not too dissimilar from a direct numerical simulation [12]. In these cases, a “wall model” is used to provide an estimate of the wall shear stress and heat flux in lieu of a no-slip closure that cannot be accurately computed. The most commonly used wall model is the equilibrium wall model, which supplies the wall-shear stress to the outer resolved flow field, assuming that thin boundary layer approximations are valid and a law of the wall is present in unresolved regions of the grid beneath the “matching location.” This model, originally conceived by Deardorff [13], is based on the constant stress layer arguments [14] and has been successfully used beyond the canonical turbulent channel and zero-pressure gradient boundary layers in *a-posteriori* LES. Recently, it was shown that wall-modeled LES with the equilibrium wall model correctly predicts the lift, pitching moment, and drag for a full aircraft system near stall conditions [15, 16]. Despite the fact that this model is formally invalid in the presence of strong pressure gradients, it has been reasoned that the equilibrium approximations are admissible if the “matching location” is sufficiently close to the wall [17]. A tighter bound on the magnitude of these errors with resolution requirements that scale locally with  $Re^{-2/3}$  has recently been established [18]. The resulting local grid point scaling,  $N \sim Re^{4/3}$ , is more restrictive than prior estimates for wall-modeled LES, and in practice, these

---

\* rahul29@stanford.edu

resolution requirements would be intractable for many practical flows at higher Reynolds numbers.

There have been several non-equilibrium wall modeling approaches that have been introduced in order to relax the assumptions on the boundary layer introduced by equilibrium wall stress approximations [19–22]. Balaras et al. [20] included the unsteady, convective, and pressure gradient terms in their equations for the wall-parallel flow to solve the thin boundary layer equations, thus making a “zonal model”. Wang and Moin [19] then proposed a model without including the convective terms. Later, Hickel [21] showed that the pressure gradient and the convective terms play a similar role and should be included together. Importantly, all these models utilized an equilibrium closure for the Reynolds shear stresses in their thin-boundary layer equations. Park and Moin [22, 23] developed an unsteady 3D RANS equation-based wall model where the eddy viscosity used to model the Reynolds stresses is computed dynamically by accounting for the effects of the resolved stresses on the skin friction. The requirement for the generation of a 3D embedded RANS mesh and interpolatory closures between the LES grid and the near-wall RANS mesh imparts significant complexity to the construction of the model and has limited its deployment in complex geometries. Moreover, improvements offered by such an approach depend on the accuracy of RANS models in adverse pressure gradient regimes, including separation. While the coupling with the interior LES can reduce the RANS modeling burden, RANS models alone have struggled in predicting flows with separation [24]. This suggests that the mere inclusion of non-equilibrium effects into the wall model does not necessarily lead to more accurate solutions. Kamogawa et al. [25] formulated the first non-equilibrium-based wall model that is completely local in the wall-parallel plane while accounting for both the convective and the pressure gradient terms. However, the authors observed marginally worse predictions of the wall-shear stress compared to the standard equilibrium wall model for a boundary layer with a blowing and suction-based top wall to induce flow separation as in Na and Moin [26].

Thus, there remains a need for improvements in-wall models for LES in flows experiencing boundary layer separation. There have also been observations of non-monotonic convergence upon grid refinement in the prediction of the size of turbulent separation bubbles depending on the choices of subgrid-scale and wall models [7, 27, 28]. Accurate solutions can be obtained, but the required grid resolutions may engender prohibitive resolution requirements in more complex flow settings. The Reynolds number scaling of the wall stress errors advanced in Agrawal et al. [18] suggests the fundamental issue remains the incorporation of the effects of imposed pressure gradients. The theoretical analysis suggests that these errors are significant when the velocity scale imposed by the pressure gradient ( $u_p^3 = \frac{\nu}{\rho} \frac{dP}{dx}$ ) is larger than the near-wall friction velocity ( $u_\tau$ ), and when the LES grid resolution ( $\Delta$ ) is resolved with respect to friction velocity length scale ( $\Delta u_\tau / \nu \sim O(1)$ ) but unresolved with respect to the pressure gradient ( $\Delta u_p / \nu \gg 1$ ). These conditions are experienced in the vicinity of a separation point at high Reynolds numbers.

Finally, we also note that there are alternative modeling strategies for the modeling of the unresolved near-wall effects that do not make a direct appeal to the thin boundary layer approximation framework. These include alternative formal boundary conditions [10, 29, 30] or purely data-driven approaches [31]. As this work investigates assumptions in the closure of the thin boundary layer equations, we do not make any direct comparisons against any of these approaches.

The rest of this article is written as follows: Section II describes the governing equations of LES, the subgrid-scale model used in this work, and a brief discussion of the computational solver. Section III proposes a wall model that includes both the pressure-gradient and convective terms. Section IV demonstrates the importance of capturing the effects of convective and pressure-gradient terms in wall-modeled LES of non-equilibrium flows in an *a-priori* sense. Sections V and VI present *a posteriori* validations of the proposed model on the Boeing speed bump and transonic Bachalo-Johnson bump. Finally, conclusions are offered in Section VII.

## II. COMPUTATIONAL METHODOLOGY

### A. Governing Equations

In this work, the filtered, large-scale field variables (such as velocity and pressure) in LES are denoted by  $\bar{f}$ , and their corresponding Favre average is denoted by  $\tilde{f}$ . The governing equations of the large-scale flow field are given by,

$$\frac{\partial \bar{p}}{\partial t} + \frac{\partial(\bar{\rho} \tilde{u}_i)}{\partial x_i} = 0 \quad (1)$$

$$\frac{\partial(\bar{\rho} \tilde{u}_i)}{\partial t} + \frac{\partial(\bar{\rho} \tilde{u}_j \tilde{u}_i)}{\partial x_j} = -\frac{\partial \bar{p}}{\partial x_i} + \frac{\partial(\mu \tilde{S}_{ij}^d)}{\partial x_j} - \frac{\partial \tau_{ij}^{sgs}}{\partial x_j}, \quad (2)$$

and

$$\frac{\partial \bar{E}}{\partial t} + \frac{\partial(\bar{E} \tilde{u}_j)}{\partial x_j} = -\frac{\partial(\bar{p} \tilde{u}_i)}{\partial x_i} + \frac{\partial(\mu \tilde{S}_{ij}^d \tilde{u}_i)}{\partial x_j} - \frac{\partial(\tau_{ij}^{sgs} \tilde{u}_i)}{\partial x_j} - \frac{\partial Q_j^{sgs}}{\partial x_j} + \frac{\partial}{\partial x_j} \left( \kappa \frac{\partial \bar{T}}{\partial x_j} \right), \quad (3)$$

where,  $\bar{E} = \bar{\rho} \bar{e} + 0.5 \bar{\rho} \tilde{u}_i \tilde{u}_i$  is the sum of the resolved internal,  $e$ , and kinetic energies,  $\rho$  is the density,  $T$ , is temperature,  $\mu(T)$  is viscosity, thermal conductivity is  $\kappa(T)$  and velocity vector  $\vec{u} = \{u_1, u_2, u_3\}$ .  $\tilde{S}_{ij}^d$  is the deviatoric part of the resolved strain-rate tensor. The relationship between the temperature and the molecular viscosity is assumed to follow a power law with an exponent of 0.75. A constant molecular Prandtl number approximation ( $Pr = 0.7$ ) is used to obtain the thermal conductivity. Two additional terms,  $\tau_{ij}^{sgs}$  and  $Q_j^{sgs}$  require modeling closure. The subgrid stress tensor,  $\tau_{ij}^{sgs}$  is defined as  $\tau_{ij}^{sgs} = \bar{\rho}(\tilde{u}_i \tilde{u}_j - \tilde{u}_j \tilde{u}_i)$ . Similarly,  $Q_j^{sgs} = \bar{\rho}(\tilde{e} \tilde{u}_j - \tilde{e} \tilde{u}_j)$  is the subgrid heat flux. The dynamic, tensorial coefficient subgrid-scale model [7] is used in the entirety of this work to model the unresolved scales of motion. The subgrid heat flux is modeled using the constant turbulent Prandtl number approximation ( $Pr_t = 0.9$ ).

## B. Numerical solver and gridding practices

The simulations presented in this article were performed using an explicit, unstructured, finite-volume solver, charLES, which solves the compressible Navier-Stokes equations as described in the preceding subsection. This code is 2<sup>nd</sup>-order accurate in space, and 3<sup>rd</sup>-order accurate in time, and utilizes Voronoi diagram-based grids. More details of the solver and validation cases can be found in Goc et al. [15, 16], Brès et al. [32], Agrawal et al. [33]. Formally skew-symmetric operators on unstructured grids are derived and used to conserve kinetic energy in the inviscid, zero Mach number limit in the current simulations. The numerical discretization also approximately preserves entropy in the inviscid, adiabatic limit. The computational grids employed in this work are based on a Voronoi diagram generated from a hexagonally close-packed lattice. In this work, control volumes are refined isotropically by factors of two in the layers near the boundaries during grid refinement studies.

## III. PROPOSED NEAR-WALL MODEL

In this section, a new wall model is proposed to improve the prediction of mean wall stress in the vicinity and inside of a turbulent separation bubble.

### A. Near-wall velocity scalings in flows with pressure gradients

Consider a turbulent boundary layer with an imposed mean pressure gradient. Tennekes and Lumley [34] and separately, Simpson [35] suggested that the two characteristic viscosity-driven velocity scales that may govern the near-wall dynamics of a wall-bounded flow experiencing pressure gradients are the shear velocity,  $u_\tau^-$  and pressure-gradient based velocity,  $u_p^-$ . Simpson [35] also showed that the  $|u_p^-|$  scaling is representative of the “backflow velocity” in the vicinity and inside the separation bubble aft of the turbulent flow over a backward-facing step. Stratford [36] used mixing layer arguments to hypothesize a square-root power law velocity scaling (in terms of  $u_p^-$ ) in the inner region of a flow at the point of separation. In the absence of a pressure gradient, the flow can be considered to be “under-equilibrium”, or the friction velocity governs the near-wall dynamics. Similarly, the other limit is obtained near a separation point when  $u_\tau^- \rightarrow 0$  and the “non-equilibrium” effects due to the pressure-gradient govern the near-wall dynamics [36]. The two velocity scales are defined as

$$u_{\tau,i} = \text{sign}(U_i) \left[ \frac{\mu}{\rho} \frac{\partial |U_i|}{\partial y} \Big|_{y=0} \right]^{1/2} \quad \text{and} \quad u_{p,i} = \text{sign} \left( \frac{\partial P}{\partial x_i} \right) \left[ \frac{\nu}{\rho} \left| \frac{\partial P}{\partial x_i} \right| \right]^{1/3} \quad (4)$$

where  $y$  denotes the wall normal direction, and  $i \in \{1, 2, 3\}$  are the cardinal directions. Note that repeated indicies in Equation 4 does not imply summation. These two velocity scales can act along complementary directions or compete against each other, which may lead to four different conditions,

1. Case I:  $\vec{u}_p \cdot \vec{u}_\tau > 0$ ;  $|\vec{u}_p| < |\vec{u}_\tau|$
2. Case II:  $\vec{u}_p \cdot \vec{u}_\tau > 0$ ;  $|\vec{u}_p| > |\vec{u}_\tau|$
3. Case III:  $\vec{u}_p \cdot \vec{u}_\tau < 0$ ;  $|\vec{u}_p| < |\vec{u}_\tau|$
4. Case IV:  $\vec{u}_p \cdot \vec{u}_\tau < 0$ ;  $|\vec{u}_p| > |\vec{u}_\tau|$

For cases I and II, the pressure gradient is adverse with respect to the skin friction, and vice versa for cases III and IV. In cases I and III, the skin friction dominates the pressure gradient effects, and hence, the equilibrium conditions are presumably only weakly violated. However, in cases II and IV, the pressure gradient effects are dominant even in the viscous sublayer (as defined by  $\frac{d}{dy} \left( \nu \frac{du}{dy} \right) = 0$ ), and a wall model that only relies upon these assumptions is not justifiable since the time scale set by the pressure gradient is faster and dominates the one from the skin friction. In the limit of a strong enough pressure gradient, Case II also represents a flow undergoing imminent separation.

Next, we make estimates for a region where the wall closure would need to be modified from the standard equilibrium approximations even outside the viscous sublayer by comparing the  $|\vec{u}_p|$  and  $|\vec{u}_\tau|$  velocity scales. Under the statistically stationary conditions, the Lagrangian integral terms that appear in the integrated streamwise momentum equations are comprised of the combined effect of the convective and the pressure gradient terms, the integrated total shear term ( $\int_0^{x^+} \tau_y^+ dx^+ = \int_0^{x^+} \left( \frac{dU^+}{dy^+} - \overline{u^{+'}v^{+'}} \right) dx^+$ ), and the turbulent transport term ( $\int_0^{x^+} \int_0^{y_1^+} \frac{du^{+'}u^{+'}}{dx'^+} dy'^+ dx'^+$  where  $(\dots)_1$  represents the value at the wall-normal location,  $y_1$ ). In this analysis, it is assumed that the pressure gradient remains nearly constant from the wall up to the matching location ( $\frac{dP}{dy}|_w \approx 0$ ) and the turbulent transport term can be ignored. Wei et al. [37] showed that even for boundary layers approaching separation, these two assumptions can lead to approximately correct description of the skin friction. The resulting approximate balance is given as follows,

$$\frac{\int_0^{x^+} \tau_y^+ dx'^+}{\int_0^{x^+} dx'^+} \approx 1 + \frac{\int_0^{x^+} \int_0^{y_1^+} \left( \frac{|\vec{u}_p^3|}{|\vec{u}_\tau^3|} + u^+ \frac{du^+}{dx^+} + v^+ \frac{dv^+}{dy^+} \right) dy'^+ dx'^+}{\int_0^{x^+} dx'^+} \quad (5)$$

where the integrand in the denominator is 1 because the system has been represented in the conventional inner viscous units (using  $u_\tau, \nu$ ). The integral on the right side of this equation is referred to with the symbol,  $\mathcal{H}$ , in the remainder of this article. Equation 5 suggests that the constant stress layer assumption invoked in the equilibrium wall model may incur large errors when the second term on the right-hand side becomes large. It is, however, cautioned that this term becoming small only implies that the shear stress at an off-wall location and the wall stress balance in an integrated sense, not locally everywhere. Following Kamogawa et al. [25], and replacing their model expression for the convective terms ( $u \frac{du}{dx} + v \frac{dv}{dy} \approx -\frac{dP}{dx} \Big|_1 \frac{u_{inner}^2}{U_1^2}$  and  $u_{inner}$  is the velocity profile below  $y = y_1$ ), the right side of Equation 5 can be rearranged as,

$$\mathcal{H} \approx \frac{\int_0^{x^+} \frac{|\vec{u}_p^3|}{|\vec{u}_\tau^3|} \left[ \int_0^{y_1^+} dy^+ - \frac{\int_0^{y_{match}^+} u_{inner}^2 dy^+}{U_1^2} \right] dx^+}{\int_0^{x^+} dx^+} \quad (6)$$

It is remarked that Kamogawa et al. [25] showed that their model form for the convective terms compares well with the DNS profiles of a flow over a flat plate with an imposed turbulent separation bubble (through blowing and suction boundary conditions) up to a  $y/\delta \approx 0.1$  where  $\delta$  is the local boundary layer thickness. For a boundary layer nearing separation, the inner mean velocity profile ( $u_{inner}$ ) is assumed to be of a composite form (see Figure 1), ensuring  $\mathcal{C}^1$  continuity based on the near-wall profile per a "half-power" law [36] and the logarithmic profile in the overlap-layer [38].

Per Agrawal et al. [18], a practically useful non-equilibrium wall model may warrant grid resolutions ( $y_1$ ) of the order  $y^p = \frac{u_p y_1}{\nu} \geq \mathcal{O}(10)$ . In this limit, the numerator of Equation 6 can be simplified such that

$$\mathcal{H} \approx \frac{\int_0^{x^+} \frac{|\vec{u}_p^3|}{|\vec{u}_\tau^3|} \left[ \int_0^{y_1^+} dy^+ - \frac{\int_0^{y_1^+} u_{inner}^2 dy^+}{U_1^2} \right] dx^+}{\int_0^{x^+} dx^+} \approx \frac{\int_0^{x^+} \frac{|\vec{u}_p^3|}{|\vec{u}_\tau^3|} y_1^p [A \log(y_1^p) + B] dx^+}{\int_0^{x^+} dx^+} \leq 1 \text{ if } |y_1^p [-A \log(y_1^p) + B] \frac{|\vec{u}_p^2|}{|\vec{u}_\tau^2}| \leq \mathcal{O}(1) \quad (7)$$

where  $-A, B > 0$  are some positive, real constants such that  $-A \log(y_1^p) + B$  is a good approximation of the wall-normal integration of the velocity profile, as used in Equation 7. Thus,  $\mathcal{H}$  becomes non-negligible in the vicinity of a separation point when

$$\frac{|\vec{u}_p^2|}{|\vec{u}_\tau^2|} - \frac{\mathcal{O}(1)}{y_1^p[-A \log(y_1^p) + B]} \geq 0 \quad (8)$$

The second term on the left side of the inequality is a decreasing function in  $y_1^p$ ; we replace it with its maximum value within the range of  $y_1^p$  of interest,  $y_1^p \gtrsim \mathcal{O}(10)$ . Thus,

$$\frac{|\vec{u}_p^2|}{|\vec{u}_\tau^2|} - 1 \geq 0 \quad (9)$$

is the simplified expression used to determine the strength of the pressure-gradient, even outside the viscous sublayer. In order to allow for standard equilibrium approximations to be utilized when the resolution is sufficient for the outer LES to capture the effects of the pressure gradient (i.e., to deactivate the sensor when  $y^p \leq \mathcal{O}(10)$ ), the inequality,

$$\frac{y^p}{2} \frac{|\vec{u}_p^2|}{|\vec{u}_\tau^2|} - 1 \geq 0 \quad (10)$$

is used (derived by replacing the near-wall, "half-power" law profile of Stratford [36] in Equation 7 instead of the composite profile in Figure 1). Appendix I also discusses a connection of the proposed sensor with the critical stable viscous layer described in Nickels [38].

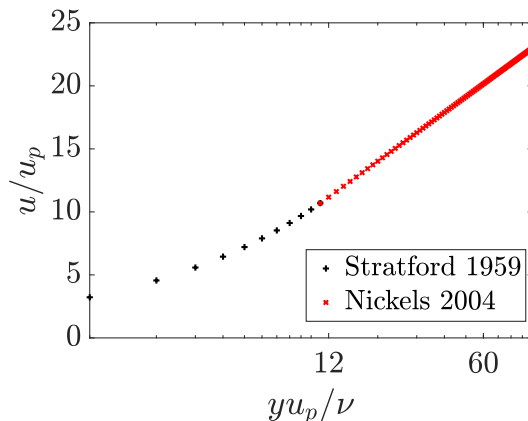


FIG. 1. The wall-normal variation of the composite,  $C^1$  continuous, mean velocity profile used to close the integral of the convective terms in Equation 12 near the separation point. The blending of the two velocity profiles occurs at  $yu_p/\nu = 12$  per the viscously "critically" stable Reynolds number arguments in Nickels [38].

## B. Wall Stress augmentation in strong non-equilibrium conditions

Once the sensor is deemed "active" (i.e., that the pressure gradient effects are deemed significant), the equilibrium wall model's predicted stress is an inaccurate stress to feed to the outer flow since the conventional constant stress layer arguments are invalid. Griffin et al. [39] showed in an *a-priori* sense that for non-equilibrium boundary layers, the stress experienced by the outer LES is different from the wall shear stress. Following this, we consider the steady Reynolds averaged boundary layer equations of LES as follows (for simplicity, the incompressible form of the governing equations is considered here),

$$\widehat{u} \frac{\partial \widehat{u}}{\partial x} + \widehat{v} \frac{\partial \widehat{u}}{\partial y} \approx -\frac{1}{\rho} \frac{d\widehat{p}}{dx} + \nu \frac{\partial^2 \widehat{u}}{\partial y^2} - \frac{\partial \widehat{u}'v'}{\partial y} - \frac{\partial \widehat{\tau}_{12}^{sgs}}{\partial y} \quad (11)$$

where  $(\widehat{\cdot})$  is the Reynolds averaged value of the LES quantities (denoted by  $(\widetilde{\cdot})$ ). Correspondingly,  $\widehat{u}$  and  $\widehat{v}$  are the streamwise and wall-normal mean LES velocities. The model of Kamogawa et al. [25], as described in the preceding section is again used to approximate the convective terms. To perform the integral containing the pressure-gradient and convective terms, an approximate value of the pressure-gradient,  $\frac{1}{\rho} \frac{d\widehat{p}}{dx}|_{match}$  is evaluated from a Taylor expansion from the quantities at the matching location. Under the assumption that  $\frac{1}{\rho} \frac{d\widehat{p}}{dy} \approx 0$  at the wall, a Taylor series approximation for the pressure gradient is likely admissible. Integrating the resulting system up to a matching location,  $y_{match}$ , with a matching velocity,  $\widehat{U}_{match}$ , gives the approximate total stress as

$$\left( \nu \frac{d\widehat{u}}{dy} - \widehat{u'v'} - \widehat{\tau_{12}^{sgs}} \right) \Big|_{y_{match}} \approx \tau_w + \frac{1}{\rho} \frac{d\widehat{p}}{dx} \Big|_{match} y_{match} \left( 1 - \frac{\int_0^{y_{match}} \widehat{u}_{inner}^2 dy}{\widehat{U}_{match}^2 y_{match}} \right) \quad (12)$$

Thus, when the sensor is “active”, the right side of Equation 12 is to be fed as the stress to the outer LES. Based on this equation, the key distinction in the present work compared to existing non-equilibrium wall models is when the sensor is “active”, we attempt modeling the wall stress using the outer LES stress at the matching location, as opposed to invoking a RANS closure for it. This approach assumes that if the sensor activates in the vicinity of the separation point, the flow is nearly resolved with respect to the friction velocity length scales (as  $y^+ \sim O(1)$ ). Wang and Moin [19] advanced a similar argument to leverage the interior LES closures, but it was applied globally without regard for local flow conditions. It was found in this work that our approach increases the wall stress (compared to the equilibrium closure) locally, just before the onset of separation, thus reducing the velocity of the near-wall flow, which in turn supports flow separation of the outer LES. Finally, the ratio  $\frac{\widehat{u}_{inner}^2}{\widehat{U}_{match}^2}$  is modeled using the composite velocity profile constructed in Figure 1. Further, consider the following application of the Cauchy-Schwartz inequality,

$$1 - \frac{1}{\widehat{U}_{match}^2 y_{match}} \int_0^{y_{match}} \widehat{u}_{inner}^2 dy \leq 1 - \frac{1}{y_{match}^2} \left( \int_0^{y_{match}} \frac{\widehat{u}_{inner}}{\widehat{U}_{match}} dy \right)^2 \quad (13)$$

If an error (say  $\chi\%$ ) is made in invoking a form of the mean velocity profile (under the assumption of a nearly uniform distribution of the error from  $y = 0$  to  $y = y_{match}$ ), then the error in the model form of Kamogawa et al. [25] scales as  $\chi^2\%$  which is smaller than the error in the wall-stress ( $\chi\%$ ). Thus, the choice of the model form for the convective terms is expected to produce smaller errors than the velocity profile used within the model form.

### C. Expected grid-point scaling with Reynolds number

Prior studies developing non-equilibrium wall models [11, 19, 20, 22, 25, 31, 39, 40] have not estimated the required grid-point scaling to perform wall-modeled LES of separated turbulent flows. Recently, Agrawal et al. [18] showed using a simplified Green’s function solution near a separation point that flow length scales “in equilibrium” for a separating boundary layer shrink with Reynolds number as  $Re^{-2/3}$ . Thus, for a computational code employing a nested-grid structure, the total number of grid points ( $N_{cv}$ ) for performing wall-modeled LES of turbulent boundary layers exhibiting smooth-body separation using an equilibrium wall closure scale as  $N_{cv} \propto Re^{4/3}$ .

Based on the experimental observations of Jovic and Driver [41], Adams [42], Devenport and Sutton [43] for the flow over a backward step, the peak of the skin-friction scales as  $Re^{-1/2}$  in the separated flow region. Assuming this is a representative Reynolds number scaling in the vicinity of the separation point for other flows exhibiting a separation as  $Re \rightarrow \infty$ ,  $\mathcal{H}$  term in Equation 7 scales as,

$$\text{At the matching location, } \mathcal{H} \sim y^p \frac{|\overline{u_p^2}|}{|\overline{u_\tau^2}|} \sim y Re^{\frac{1}{2}} \text{ as } Re \rightarrow \infty \quad (14)$$

Thus, to capture the non-equilibrium component of the stress accurately independent of the Reynolds number, the grid resolution,  $y_{match} \sim Re^{-1/2}$ . This also recovers the linear grid-point scaling of wall-modeled LES with Reynolds number previously derived for flat-plate, equilibrium flows [12]. This expectation will be briefly tested in the *a-posteriori* section of this article.

#### IV. A PRIORI PERFORMANCE OF PROPOSED MODEL

In the preceding section, a closure model including pressure-gradient and convective terms in wall-modeled LES of non-equilibrium flows was presented. In this section, we discuss in an *a-priori* sense the importance of the pressure-gradient and convective terms, thus explaining the need to include the non-equilibrium component of the stress supplied to the outer flow. The error encountered in the stress supplied to the outer flow from the equilibrium wall model (which assumes a constant stress layer between the wall and the matching location) is compared with that from the proposed model (Equation 12) in an adverse pressure gradient flat-plate boundary layer [44] and over non-equilibrium airfoil flows [45, 46].

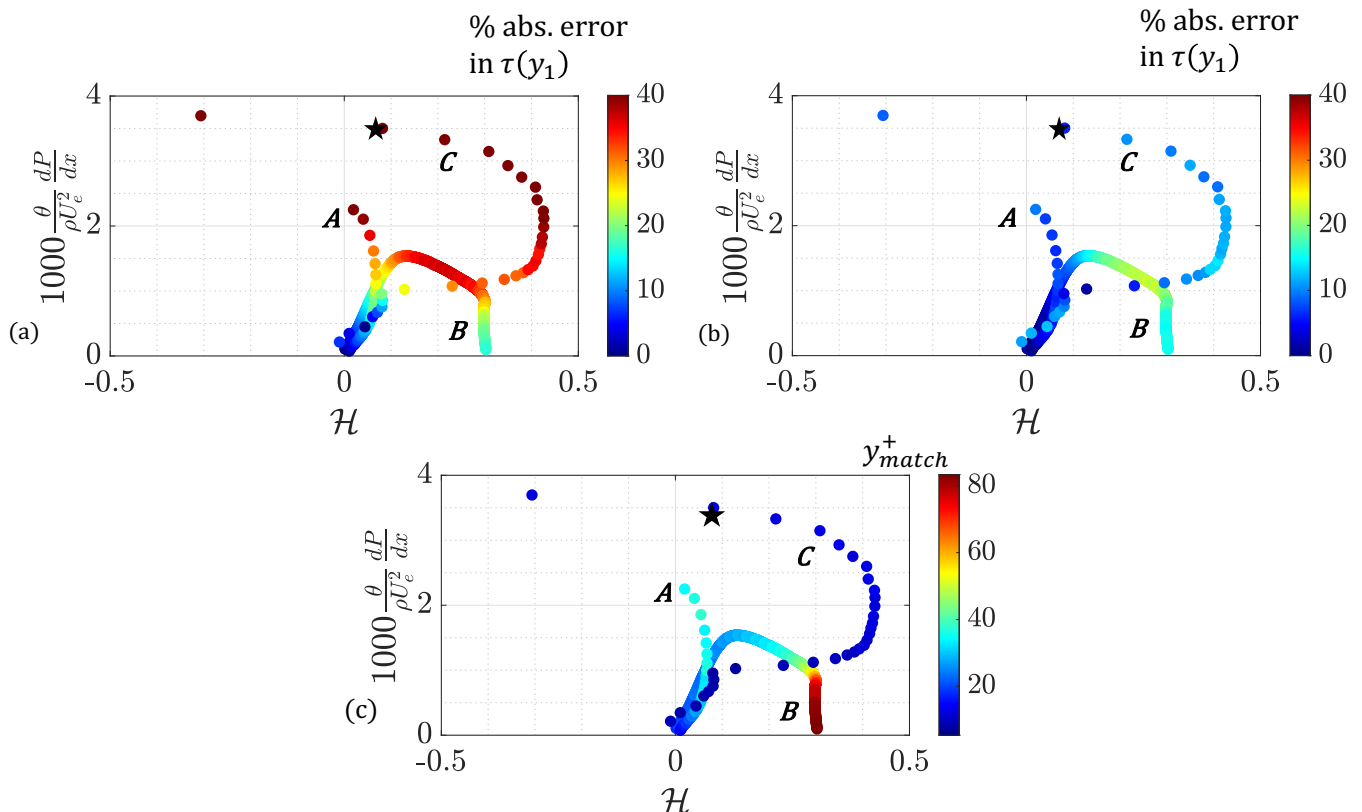


FIG. 2. *A-priori* absolute percentage error distribution in the prediction of the total stress at the matching location as a function of  $\mathcal{H}$  (see Equation 7) and the Alber parameter  $(\theta/(\rho U_e^2)dP/dx)$  for a fixed matching location in outer units,  $y_{match}/\delta = 0.1$ , for (a) equilibrium wall model in Lehmkuhl et al. [47] and (b) proposed model in Equation 12. Subfigure (c) denotes the height of the matching location in viscous units. The capital letters denote the data points from different flows: Data-series A corresponds to streamwise stations in flow over a NACA 0012 airfoil studied in Tanarro et al. [46]. Similarly, data-series B corresponds to a flat-plate boundary layer at  $U_e \sim x^{-0.13}$  case studied in Bobke et al. [44]. Data-series C corresponds to stations of flow over a NACA 4412 airfoil studied by Vinuesa et al. [45]. The starred point is a sample point chosen to aid the interpretability of this plot. This data point corresponds to NACA 4412 flow at  $\Lambda \approx 0.0035$ ,  $\mathcal{H} \approx 0.1$  at a matching location,  $y_{match}^+ \approx 13$ . The percentage error in the shear-stress prediction at this point is 60% when employing the equilibrium wall model, and 12% when employing the proposed model.

Figure 2 shows the absolute errors in the prediction of the stress supplied to the outer solution at the matching location based on the equilibrium closure and the proposed closure for a fixed matching location,  $y_{match}/\delta = 0.1$ . The abscissa for this plot is  $\mathcal{H}$  term from Equation 7, and the ordinate represents the flow-separation parameter of Alber [48]. This parameter is useful in identifying the outer-scale behavior of the boundary layer and also its proximity to flow separation (the threshold suggested by Alber [48] is  $\Lambda = \theta/(\rho U_e^2)dP/dx = 0.004$ ). It is apparent in Figure 2(a) that the errors incurred by the equilibrium closure generally grow as  $\mathcal{H}$  increases. However, as depicted in Cases A and C, the errors also exhibit a non-monotonic behavior with  $\mathcal{H}$  as  $\Lambda \rightarrow 0.004$  (intermittent flow separation). This implies that even at a constant outer resolution ( $y_{match}/\delta = \text{constant}$ ), the validity of the constant stress layer below the matching location can increase or decrease non-monotonically along the streamwise direction. On the contrary,

Mesh	$N_{cv}$	max $\Delta/L$	min $\Delta/L$
Coarse	3 Mil.	$1 \times 10^{-2}$	$1.3 \times 10^{-3}$
Medium	12 Mil.	$1 \times 10^{-2}$	$6.3 \times 10^{-4}$
Fine	52 Mil.	$1 \times 10^{-2}$	$3.1 \times 10^{-4}$

TABLE I. Mesh parameters for the quasi-DNS based spanwise-periodic case for the flow over the Boeing speed bump.

in Figure 2(b), the proposed wall model (in Equation 12) produces smaller errors and also does not exhibit the non-monotonic behavior observed with the equilibrium closure. Figure 2(c) denotes the height of the matching location in viscous units; for cases A-C, as  $\Lambda$  increases, the matching height decreases as the flow nears separation. Case B represents a flow with a freestream velocity profile governed by a power law ( $U_e \sim x^{-0.13}$ ) studied by Bobke et al. [44]; the proposed model produces errors that are smaller than the equilibrium closure.

## V. WALL-MODELED LES OF FLOW OVER A GAUSSIAN BUMP

The development of CFD practices and models that predict smooth body separation was considered as a pacing item in the CFD 2030 Vision report [24]. This section describes a canonical case exhibiting this phenomenon in the flow over the NASA/Boeing speed bump [49–52]. In laboratory experiments, the solid body is shaped as a Gaussian in the streamwise direction and has tapered side-shoulders in the spanwise direction. The flow over the speed bump experiences a strong favorable pressure gradient followed by a strong adverse pressure gradient on the fore and aft sections of the bump, respectively. Williams et al. [49] showed that at high Reynolds numbers, a turbulent separation bubble is formed on the aft side of the bump. Both the measurements of the skin friction and pressure drag in Williams et al. [49], Gray et al. [51] also suggested an approximate Reynolds number independence for  $Re_L \geq 1.8 \times 10^6$ .

Uzun and Malik [53] performed a quasi-DNS (resolution of the outer part of the boundary layer resembles an LES) of this flow for a simplified, spanwise periodic variant of the geometry. Their results compare well with those from the experiments of Williams et al. [49], Gray et al. [50] at the midspan of the experimental configuration, and hence, the former is studied in this work. Within the context of wall-modeled LES, Whitmore et al. [30], Zhou and Bae [54] have demonstrated the sensitivity of the prediction of flow separation to the choice of the subgrid-scale model, meshing topology, and the wall model. The “building-block” machine-learning-based wall model of Arranz et al. [55] led to reasonable predictions of the separation bubble in this flow; however, they did not perform enough grid-refinements to exactly match the reference  $C_p$  and  $C_f$  values. Agrawal et al. [7] used their non-Boussinesq subgrid-scale model with an equilibrium wall closure to produce accurate predictions of the separation bubble, but only on the most refined grids (finer than those simulated in Arranz et al. [55]).

For this flow, the primary quantities of interest are the skin friction coefficient ( $C_f$ ) and pressure coefficient ( $C_p$ ) which are defined as

$$\frac{C_f}{2} = \frac{\tau_w}{\rho_\infty U_\infty^2} \quad \text{and} \quad \frac{C_p}{2} = \frac{p - p_{\text{ref}}}{\rho_\infty U_\infty^2}. \quad (15)$$

where  $U_\infty$ ,  $\tau_w$ ,  $p$  and  $p_{\text{ref}}$  are the mean free-stream velocity, wall-stress, wall pressure, and the upstream reference pressure in the zero-pressure region of the flow respectively. Figure 3 provides a schematic of the simulation setup for this flow.

For the spanwise periodic case, the bump surface is defined by an analytical expression,  $h(x, z)$ , written as

$$h(x) = \frac{h_0}{2} e^{-(x/x_0)^2}, \quad (16)$$

where  $x$  is the streamwise direction and  $h_0 = 0.085L$  is the maximum height of the bump; and  $x_0 = 0.195L$  controls the Gaussian decay of the surface along the  $x$  direction. The Reynolds number,  $Re_L$  for this flow is defined in terms of the freestream velocity  $U_\infty$  and the bump width,  $L$ . The computational grids and the grid-refinement practices are maintained to be the same as those in Agrawal et al. [7, 56], and some details are provided in Table I.

In this work, we first study the  $Re_L = 2 \times 10^6$  flow to match the aforementioned quasi-DNS [53]. Based on Agrawal et al. [57] who showed that the separation tendency of this flow is roughly independent of the exact inlet boundary condition, we feed a plug-flow at the inlet ( $x/L = -1.0$ ). This leads to a finite flow development length (similar to the previous results of Agrawal et al. [7], Whitmore et al. [30], Arranz et al. [55]). However, by  $x/L = -0.6$



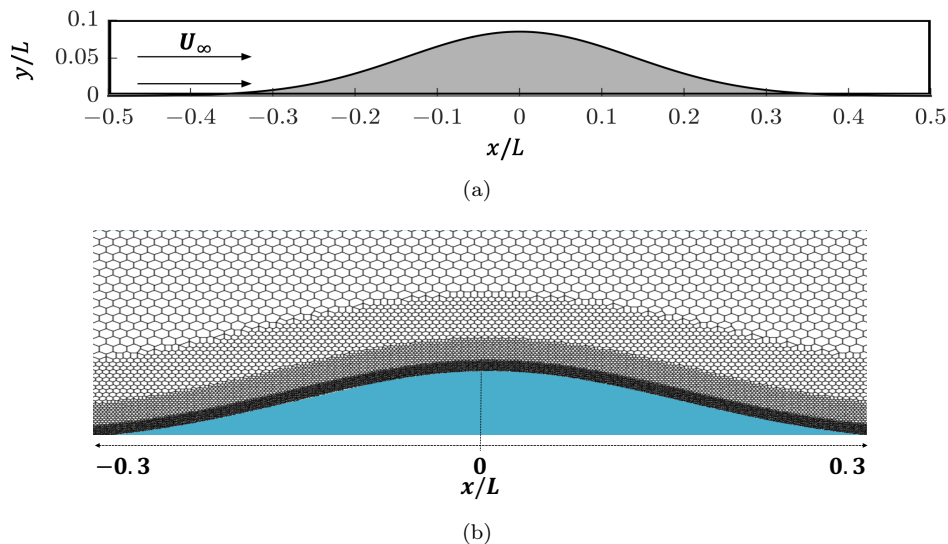


FIG. 3. (a) A schematic of the simulation setup for the flow over the spanwise periodic NASA/Boeing speed bump at  $Re_L = 2 \times 10^6$ . The spanwise direction spans between  $0 \leq z/L \leq 0.08$  and the top wall is at  $y/L = 1.0$ . (b) Cross section of the “coarse” grid arrangement (details in Table I). Only the lower half of the vertical extent of the domain is shown. The top half is meshed uniformly up to the top wall. Three layers of isotropic refinement are visible adjacent to the bump surface.

(well upstream of the bump), the skin friction agrees with the quasi-DNS. Free-stream conditions are set at the top boundary. A non-reflecting characteristic boundary condition with constant pressure is applied at the outlet (located at  $x/L = 2.5$ ). The flux at the bump wall is provided using a wall model.

### A. Predictions with proposed wall-model

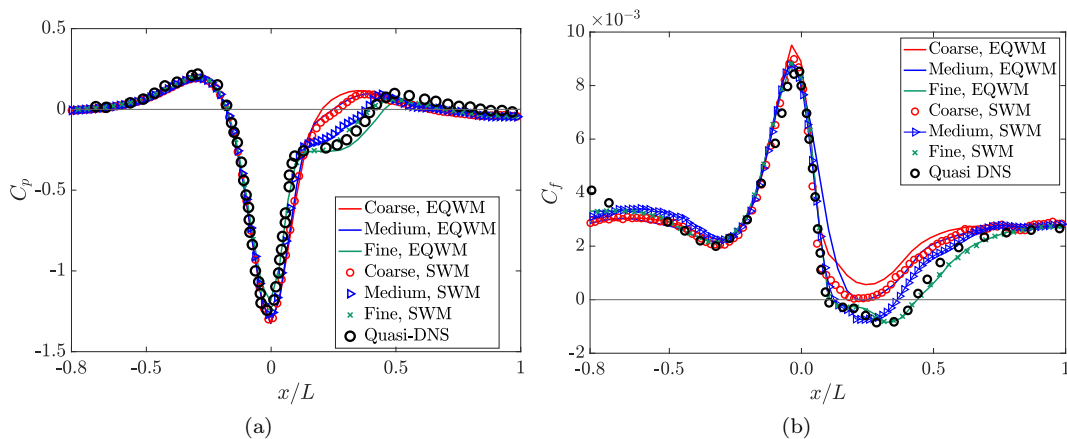


FIG. 4. Streamwise distribution for the spanwise-periodic bump at  $Re_L = 2 \times 10^6$  of (a) the surface pressure coefficient and (b) the surface friction coefficient. The proposed non-equilibrium wall model is applied, and three mesh resolutions are shown. The black symbols represent the quasi-DNS of Uzun and Malik [53]. Here, SWM refers to the proposed sensor-based wall model in this work. The results corresponding to DTCSM/EQWM models were reproduced from Agrawal et al. [7] with permission. Note that in subfigure (a), the blue solid line (medium grid, EQWM result) nearly overlaps with the red symbols (coarse grid, SWM result). This also holds in subfigure (b) for  $x/L \gtrsim 0.25$  region.

Figures 4(a) and 4(b) provide a comparison between the predictions of the surface pressure and the skin-friction from the standard equilibrium wall model [47] (denoted EQWM) and the proposed wall model (denoted SWM). This comparison is also made across a sequence of grid-refinements from “coarse” to “medium” and “fine” (detailed in Table

I). For both these figures, the predictions from the proposed wall model compare more favorably with the reference data than those from the equilibrium wall model. The equilibrium wall model predicts a flow separation on the finest grid only; however, with the proposed model, a separation bubble is predicted even on the medium grid (marked by the flattening of the  $C_p$  curve or the occurrence of negative  $C_f$ ). Secondly, the monotonic approach of WMLES with grid-refinement towards reference data remains preserved with the proposed model. In line with the results reported in Agrawal et al. [7], the skin-friction peak (which occurs when the inviscid pressure gradient flips its sign) is well captured for both wall models. Finally, the upstream skin friction between  $-0.6 < x/L < -0.3$  is more accurate than those in other studies that employ similar inflow conditions but different wall-closures [30, 55, 58]. Appendix II presents an *a-posteriori* sensitivity of the prediction of wall-modeled LES to the choice of the order of magnitude of the second term in Equations 8-9.

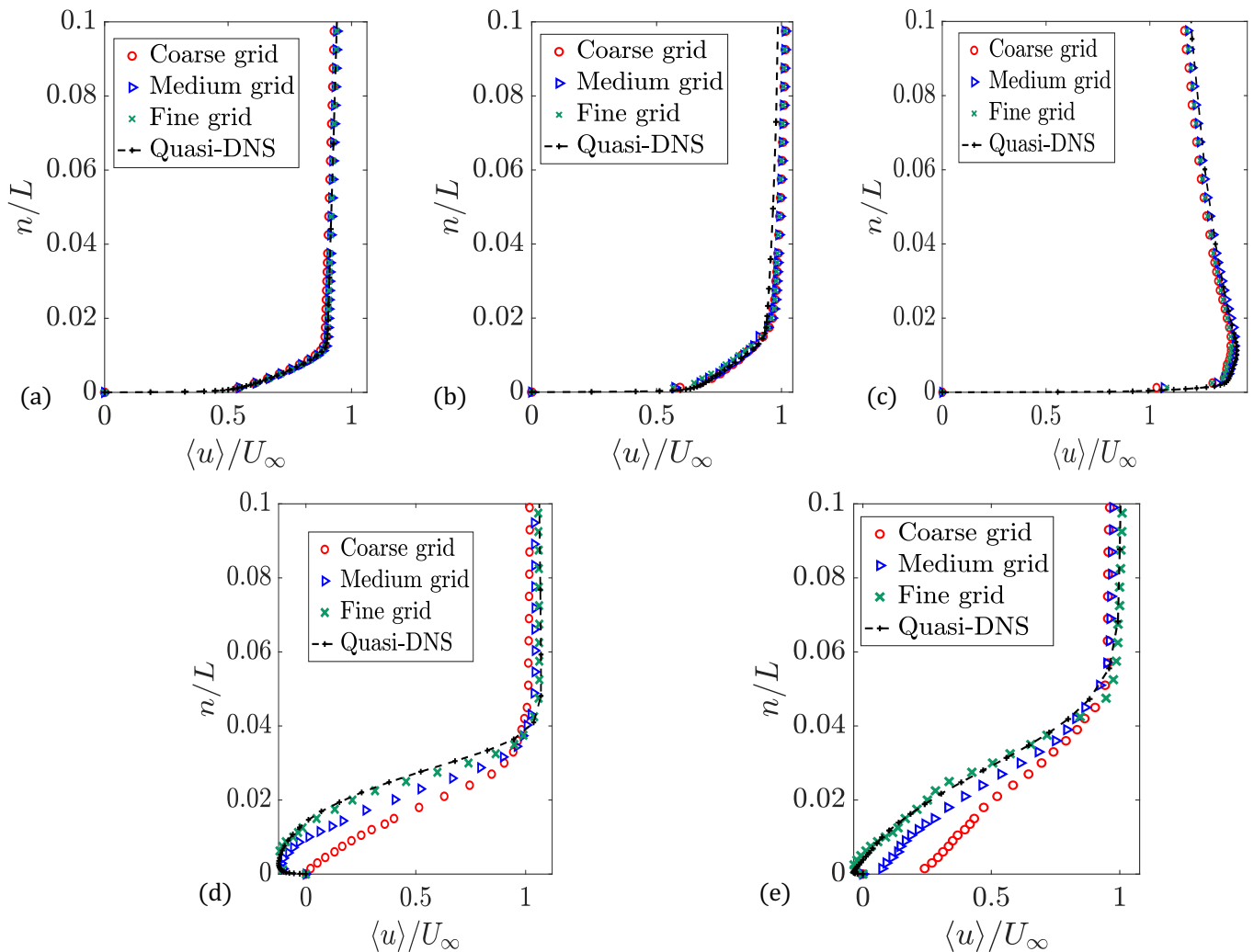


FIG. 5. The nondimensional streamwise velocity profiles,  $\langle u \rangle / U_\infty$  at (a)  $x/L = -0.4$ , (b)  $x/L = -0.2$ , (c)  $x/L = 0.0$ , (d)  $x/L = 0.2$ , and (e)  $x/L = 0.4$  for flow over the Boeing speed bump at  $Re_L = 2 \times 10^6$ . The quasi-DNS refers to the study of Uzun and Malik [53]. The predictions are shown across the grid-refinement sweep for the tensorial subgrid-scale model and the proposed wall model combination.

The quality of the solutions is further probed by comparing the mean streamwise velocity profiles from wall-modeled LES to the quasi-DNS. In Figure 5, the profiles at five stations ( $x/L = -0.4, -0.2, 0.0, 0.2, 0.4$ ) are plotted. For subfigures (a)-(c), which correspond to the pre-separation region, good and largely grid-insensitive agreement of the mean profiles with quasi-DNS is observed. In the post-separation region ( $x/L \geq 0.1$ , subfigures (d)-(e)), larger differences are observed with the agreement between wall-modeled LES and quasi-DNS improving as the grid is refined. The coarse and the medium grids predict a “faster” velocity near the wall that is consistent with the reduced flow separation compared to the fine grid.

Furthermore, the streamwise growth of the momentum thickness ( $\theta$ , refer to White [59] for more details) and the shape factor ( $H = \delta^*/\theta$ ) in these simulations is plotted in Figure 6. The predicted wall-modeled LES solutions are in good agreement with the reference data for all the grids up to  $\approx x/L = 0.05$ , beyond which the occurrence (or absence) of flow separation determines the growth of the boundary layer. On the aft side of the bump, the attached boundary layers on the coarse grid and on the equilibrium wall model's medium grid lead to a nearly constant rate of growth of the boundary layer in the  $0.1 \leq x/L \leq 0.3$  region. The adverse pressure gradient increases the shape factor up to  $x/L \approx 0.25 - 0.30$ , beyond which the pressure gradient on the attached flow becomes favorable. On the medium and fine grids employing the proposed model,  $\theta$  qualitatively follows the diminished growth (due to a negative  $C_f$  contribution in the Von-Karman integral equation). Similarly, the shape factor,  $H$ , increases rapidly beyond  $x/L = 0.10$  (the mass deficit in the boundary layer rapidly increases in the separated region). The fine grid produces more favorable solutions consistent with its  $C_p$ ,  $C_f$ ,  $\langle u \rangle$  being more accurate than the medium grid in the separated flow.

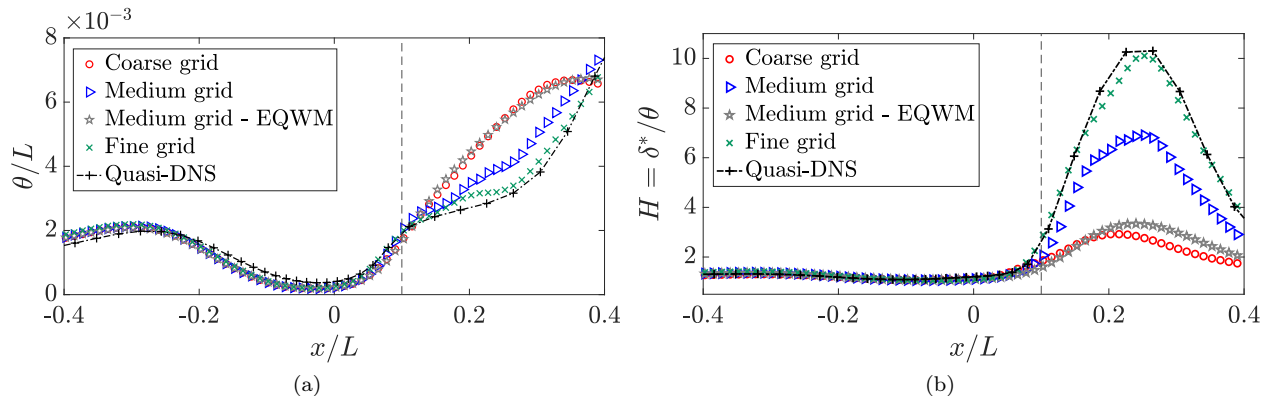


FIG. 6. The predicted streamwise dependence of (a) the momentum thickness ( $\theta$ ) and (b) the shape factor ( $H = \delta^*/\theta$ ) across the grid-refinement sequence for the flow over the Boeing speed bump at  $Re_L = 2 \times 10^6$ . The quasi-DNS refers to the study of Uzun and Malik [53]. Unless otherwise stated, the proposed wall-model in this work is employed. The vertical dashed line denotes the point of separation in the reference quasi-DNS at  $x/L = 0.1$ .

### B. Activity of the proposed sensor

Since the proposed wall model is aimed to capture non-equilibrium in the vicinity of a separation point, we expect that the proposed sensor only turns on in near separation regions. This is established in an *a-posteriori* sense by plotting the activity, denoted by  $\gamma = \frac{1+sgn(\langle \chi \rangle)}{2}$ , where  $\langle \dots \rangle$  represents the time and span averaging operator,  $\chi$  is the left side of the inequality in Equations 9-10 and  $sgn(\dots)$  is the sign function. In effect,  $\gamma$  represents the time-averaged spatial extent of the region of flow non-equilibrium as reported by the sensor. In the regions where the near-wall equilibrium assumption fails, the activity parameter  $\gamma(x/L) = 0.0$  and vice versa. Figure 7 presents the spatial distribution of  $\gamma$  across the grid-refinement sequence. This plot confirms for this flow that the sensor augments the equilibrium wall model's prediction selectively in the regions of the strong adverse pressure gradient and inside the separation bubble. Further, as the grid is refined, the sensor reacts to the local flow state, and the activity is generally reduced compared to a coarser grid. On the "fine grid", the sensor only becomes active at the mean separation point, and otherwise, the outer flow is resolved enough to largely be in equilibrium.

### C. Reynolds number scaling of grid-point requirements of wall-modeled LES

As noted before, the experiments of Williams et al. [49] and Gray et al. [51, 52] have both hypothesized an approximately Reynolds number independent extent of the separation bubble on the aft side of the bump at sufficiently high Reynolds numbers. Their experimental measurements were reported for  $1.8 \times 10^6 \leq Re_L \leq 4 \times 10^6$ . Agrawal et al. [18] performed a series of wall-modeled LES of the flow over the speed bump up to  $Re_L = 10 \times 10^6$  and reported that the results converged towards the experimental  $C_p$  trace (at  $Re_L = 2 \times 10^6$ ) in the domain. These synthetic experiments are repeated to assess the grid-resolution scaling (with Reynolds number) of *a-posteriori* wall-modeled

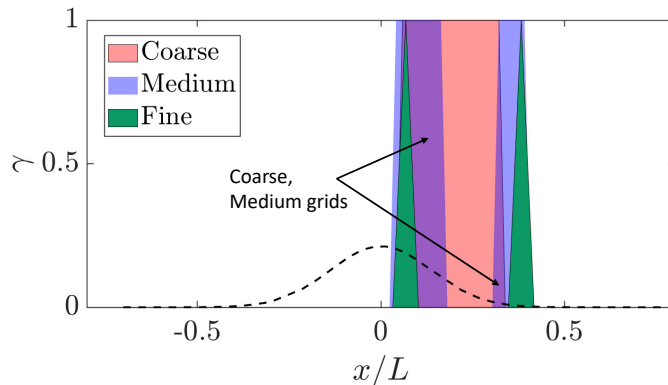


FIG. 7. The streamwise distribution of the averaged activity parameter  $\gamma$  for the Boeing speed bump flow at  $Re_L = 2 \times 10^6$ . In the regions where  $\gamma > 0$ , the sensor is active. In the experiments, the extent of the separation bubble is confined to within  $x/L = 0.1$  and  $0.4$ . The black-dashed curve represents a schematic of the bump geometry. Note that the violet color represents the regions where the sensor is active on both the coarse and the medium grids.

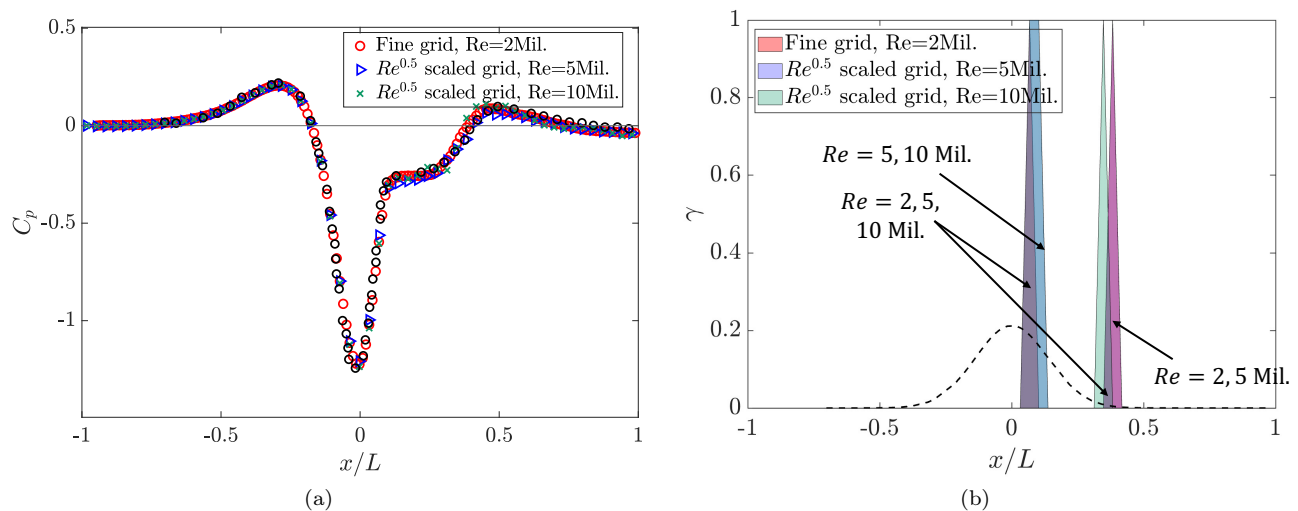


FIG. 8. Streamwise distribution of the (a) surface pressure distribution coefficient,  $C_p$ , (b) activity parameter of the sensor at the wall for the flow over the spanwise-periodic Boeing speed bump as a function of the Reynolds number. In subfigure (a), the black dots represent the  $C_p$  reported in the quasi-DNS of Uzun and Malik [53]. The fine grid at  $Re_L = 2 \times 10^6$  is considered as the base grid in this plot. In subfigure (b), the black-dashed curve represents a schematic of the bump geometry, and the arrows point to the sensor becoming active for two or all three Reynolds numbers at the same  $x/L$ .

LES employing the proposed wall model.

The fine grid for the  $Re_L = 2 \times 10^6$  flow is considered as the baseline grid. Per the scaling hypothesized in Section III(C), the grids are refined by a factor of  $Re^{1/2}$  as the Reynolds number increases. Figure 8(a) suggests that the predicted  $C_p$  also compare well with each other and with the quasi-DNS [53] at  $Re_L = 2 \times 10^6$ . Figure 8(b) confirms that the sensor reacts to the change in the Reynolds number and a larger region of flow non-equilibrium is highlighted as the Reynolds number is increased. These results suggest that at least for this flow, the *a-priori* Reynolds number scaling of the grid resolution for capturing the separation bubble is also realized *a-posteriori* with the proposed wall model.

## VI. WALL MODELED LES OF BACHALO-JOHNSON AXISYMMETRIC TRANSONIC BUMP

Bachalo and Johnson [60] conducted an experimental investigation of a canonical flow that produces a transonic shock-induced flow separation at a high chord-based Reynolds number ( $Re_c = 2.76 \times 10^6$ ), along with the adverse-

pressure gradient-induced smooth-body separation; both of which occur on the suction surface of transonic airfoils. In this experiment, an axisymmetric solid model with a spherical bump is placed in a flow with a transonic free-stream Mach number. The turbulent boundary layer that develops over the model's surface upstream of the bump interacts with the local supersonic flow over the bump, leading to the detachment of the boundary layer and flow separation. The experiments also included results at slightly different Mach numbers ( $Ma = 0.85, 0.875, 0.90$ ), which produced significantly different flow separation and recovery regions. This finding has been since corroborated in a recent set of experiments at the Sandia National Labs [61], albeit at a lower Reynolds number ( $Re_c = 1 \times 10^6$ ). We highlight that although the bump width-based Reynolds number of the Bachalo-Johnson flow is comparable to that over the Boeing speed bump, the incoming reference momentum (at  $x/c = -0.25$ ) thickness-based Reynolds number for this flow is  $Re_\theta \approx 12000$ , which is an order of magnitude larger than the flow over the Boeing speed bump ( $Re_\theta \approx 1400$ ).

Previous efforts to simulate the flow over the Bachalo Johnson bump have generally been limited to the  $Ma_e = 0.875$  case. Jespersen et al. [62] performed RANS computations using the OVERFLOW solver that did not predict flow separation. Later, Spalart et al. [63] performed scale-resolving detached eddy simulations using approximately  $\approx 400$  million control volumes. However, their solutions did not predict the flow separation either. More recently, Lv et al. [64] have accurately predicted the surface-pressure distribution by performing wall-modeled LES using a discontinuous Galerkin framework. Horstman and Johnson [65] have demonstrated the inability of RANS models to capture the sensitivity of the reattachment point to small variations in the Mach number. In this work, the sensitivity of this model to slight changes in the freestream conditions and the corresponding separation extent is examined by simulating the three slightly different Mach number flows. To the authors' knowledge, the ability of wall-modeled LES to respond to changes in Mach number in this flow has not been reported previously.

### A. Case setup and boundary conditions

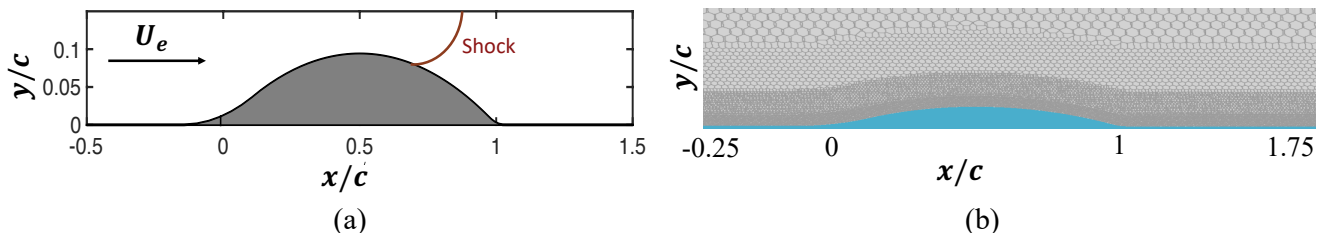


FIG. 9. A schematic of the (a) case setup and the (b) grid distribution along the streamwise direction for the transonic flow over the axisymmetric Bachalo-Johnson bump. It is highlighted that the grid is maintained to be agnostic to the location of the shock in the streamwise direction. Near-wall refinement is performed in layers of isotropically growing cells. The shock location for  $Ma_e = 0.875$  flow is approximately at  $x/c = 0.67$ .

The Reynolds number of the flow is based on the freestream velocity,  $U_e$ , and the bump chord ( $c$ ) and is equal to  $Re_c = 2.76 \times 10^6$ . The three different Mach numbers are  $Ma_e = 0.85, 0.875, 0.90$ . A plug profile is fed at the inlet (located at  $x/c = -4$ ), and the boundary layer is allowed to develop into a statistically equilibrated zero-pressure pressure gradient flow. The flow then encounters the bump at  $x/c = 0$  followed by a strong favorable pressure gradient region up to  $x/c = 0.5$ . Thereafter, the flow experiences an adverse pressure gradient before it encounters the shock ( $x/c \approx 0.67$ ) that leads to the flow separation downstream. The outlet is located at  $x/c = 10$  to allow the flow to recover from the separation. The simulation domain is a  $60^\circ$  sector of the axisymmetric geometry, with the characteristic, non-reflective boundary conditions at the outlet. Figure 9(a) shows the flow domain schematic in the near-bump region. Similarly, Figure 9(b) shows the grid distribution over the bump surface; an isotropic, layered, near-wall refinement strategy is pursued to capture the smaller scales of the flow near the wall. Finally, the grid is also maintained to be agnostic to the streamwise location of the shock to challenge the wall-modeled LES methodology. The details of the grid resolution are provided in Table II; the last column shows that in terms of the viscous length scale imposed by the pressure gradient ( $l_p$ ), this flow is under-resolved.

Mesh	$N_{cv}$	max $\Delta/c$	min $\Delta/c$	max. $\Delta/l_p$
WMLES	31 Mil.	$2.5 \times 10^{-1}$	$2 \times 10^{-3}$	$\approx 70$

TABLE II. Mesh parameter for a  $60^\circ$  sector case of the axisymmetric, transonic flow over the bump in the experiments conducted by Bachalo and Johnson [60]. Compared to the experimental boundary layer thickness in Bachalo and Johnson [60], at this grid resolution, the incoming boundary layer ( $x/c \approx -0.25$ ) contained approximately 15 grid points. In the last column,  $l_p$  denotes the viscous length scale governed by the pressure gradient term,  $l_p = \nu/u_p$ .

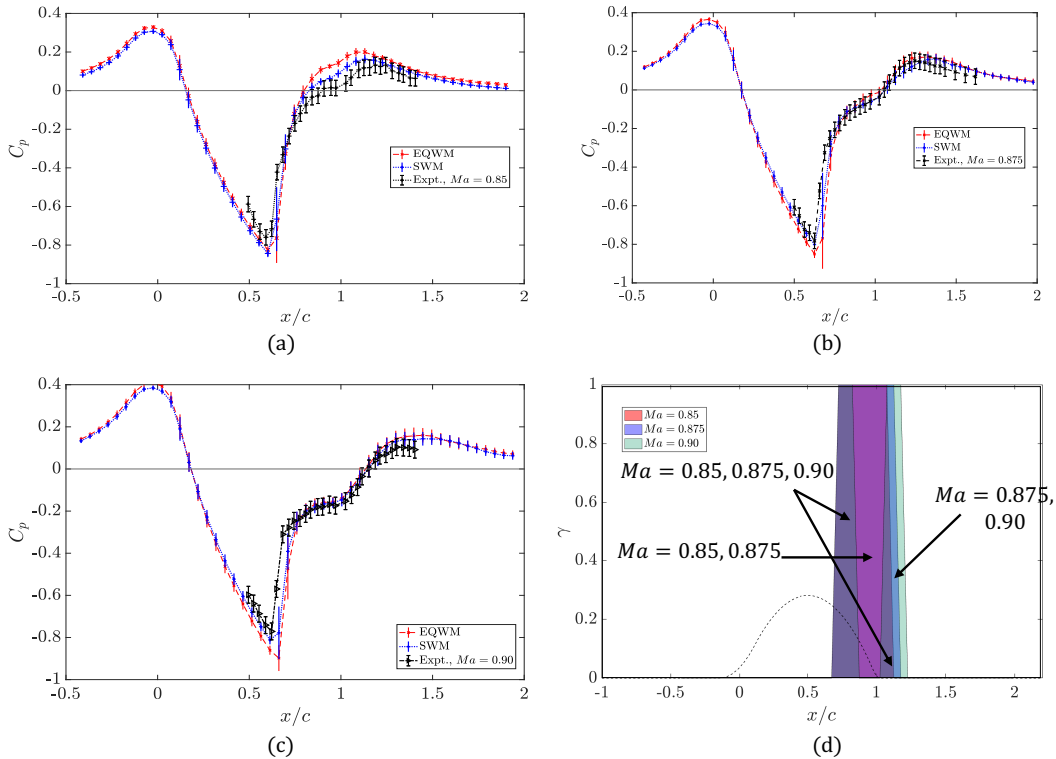


FIG. 10. A comparison of the predicted surface pressure coefficient,  $C_p$ , between the equilibrium wall model and the proposed model for the three Mach number cases, (a)  $Ma_e = 0.85$ , (b)  $Ma_e = 0.875$  and (c)  $Ma_e = 0.90$ . For reference, the  $C_p$  traces from the experiments of Bachalo and Johnson [60] are also reported. Subfigure (d) presents the activity parameter of the sensor at the wall, the black-dashed curve is a schematic of the transonic bump geometry, and the arrows point to the sensor becoming active for two or all three Mach numbers at the same  $x/c$ .

## B. Predictions with the proposed wall-model

In the original Bachalo-Johnson experiment, the streamwise trace of  $C_p$  was reported for all three Mach numbers,  $Ma_e = 0.85$ ,  $0.875$ , and  $0.90$ . In the current simulations, regardless of the varying Mach number, the same mesh, subgrid-scale, and wall model is employed. Figure 10(a)-(c) compares the prediction of the surface pressure resulting from the equilibrium wall model and the proposed model at  $Ma = 0.85$ ,  $0.875$ , and  $0.90$  respectively. At the lowest Mach number ( $Ma_e = 0.85$  in subfigure (a)), the shock is not strong enough to separate the flow, and the adverse pressure gradient downstream of the shock leads to a flow separation (constant  $C_p$  plateau) at  $x/c \approx 0.75$ . The proposed model, although slightly under-predicts the separation, is in more agreement with the experiments [60] than the equilibrium model. The predictions on a more refined grid are found to be more favorable and are presented in Appendix III. The shock is strong enough to lead to flow separation at its foot at the two higher Mach numbers in subfigures (b)-(c). Both the models reasonably predict this separation and the subsequent reattachment location (although at  $Ma_e = 0.875$ , the proposed model is slightly better than the equilibrium wall model).

The size of the separation bubble also increases with the Mach number, possibly due to an increased effect of the pressure gradient (the Von Karman integral equation suggests that the skin friction is dependent on the product of an explicit function of the pressure gradient,  $f(dP/dx)$  and the Mach number,  $Ma_e^2$ ). It was verified that the viscous

resolution of the matching location for our simulations is  $\mathcal{O}(100)$  in the upstream, zero-pressure gradient boundary layer region ( $x/c \leq 0$ ) and that simulations using a no-slip boundary condition produce inaccurate solutions. Similar to Figure 7, the activity of the proposed sensor is plotted in Figure 10(d). The sensor becomes active only at or after the foot of the shock ( $x/c \approx 0.67$ ) for all three Mach numbers, which is in line with the location of the onset of flow separation. Additionally, the sensor responds to a change in the Mach number, remaining active for a slightly larger  $x/c$  location as the Mach number increases. This is consistent with the fact that the reattachment point also moves downstream with Mach number.

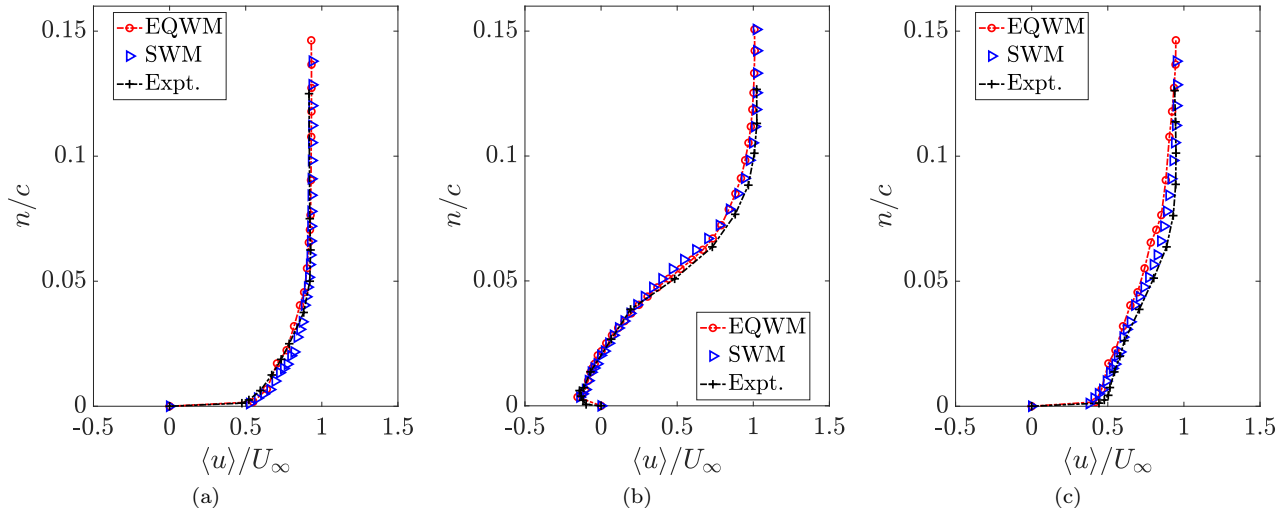


FIG. 11. Wall normal (along the direction orthogonal to the axis of the bump) profiles of the normalized streamwise velocity,  $\langle u \rangle / U_\infty$ , at (a)  $x/c = -0.25$ , (b)  $x/c = 1.00$ , and (c)  $x/c = 1.375$  for flow over the transonic Bachalo-Johnson bump at  $Re_c = 2.76 \times 10^6$  and  $Ma_e = 0.875$ . The reference experiments shown in black are from the experiments of Bachalo and Johnson [60]. The three selected locations represent the upstream region before the bump, the separated region at the foot of the bump, and the downstream region past the reattachment point, respectively.

The experiments of Bachalo and Johnson [60] provide wall-normal profiles of the streamwise-velocity at several  $x/c$  stations for the  $Ma_e = 0.875$  case. The prediction of the outer flow from wall-modeled LES is assessed using these velocity profiles. Figure 11 compares these predictions between the two models at three stations,  $x/c = -0.25$ ,  $1.00$ ,  $1.375$ , which are representative of the upstream, separated, and recovery regions, respectively. At  $x/c = -0.25$ , both models produce similarly accurate velocity profiles, which is expected as the flow is in “equilibrium”. In the separated region ( $x/c = 1.00$ ) as well, the predicted velocity profiles from both models compare well with the experiment. These profiles also reasonably predict the two inflection points, which lead to the formation of embedded shear layers (see Schatzman and Thomas [66]) in separated flows. In the post-reattachment and recovery region ( $x/c = 1.375$ ), the proposed model slightly improves the prediction of the mean velocity in comparison to the equilibrium wall model. Overall, it is concluded that the predictions of the mean velocities from wall-modeled LES are in good agreement with the reference experimental data [60].

### C. Dependence of flow separation on Mach number

Figures 12(a), (c), and (e) present contours of the time-averaged streamwise velocity for the three Mach numbers at  $0^\circ$  azimuthal angle. The green, purple, and black dashed lines correspond to the location of the shock, the point of separation, and the point of reattachment, respectively. The shock location is found to be relatively insensitive to the Mach number; however, the shock becomes more oblique, as expected, with the Mach number. The separation point for  $Ma_e = 0.85$  is slightly downstream of the two higher  $Ma_e$  cases, which separate approximately at the foot of the shock. The separated shear layer (marked by the white contours beyond the separation point) is more lifted, and then attaches with the bump wall further downstream as the Mach number increases. Figures 12 (b), (d), and (f) present the contours of the instantaneous pressure fluctuations for the flow cases at  $Ma_e = 0.85$ ,  $Ma_e = 0.875$  and  $Ma_e = 0.90$  respectively. The increasing obliqueness of the shock with the Mach number is also visible in these

figures. The separated region downstream of the shock produces larger (in magnitude) pressure fluctuations as the Mach number increases. This is due to the unsteady shedding of the shear layer, which is correlated to the formation of a larger separation bubble.

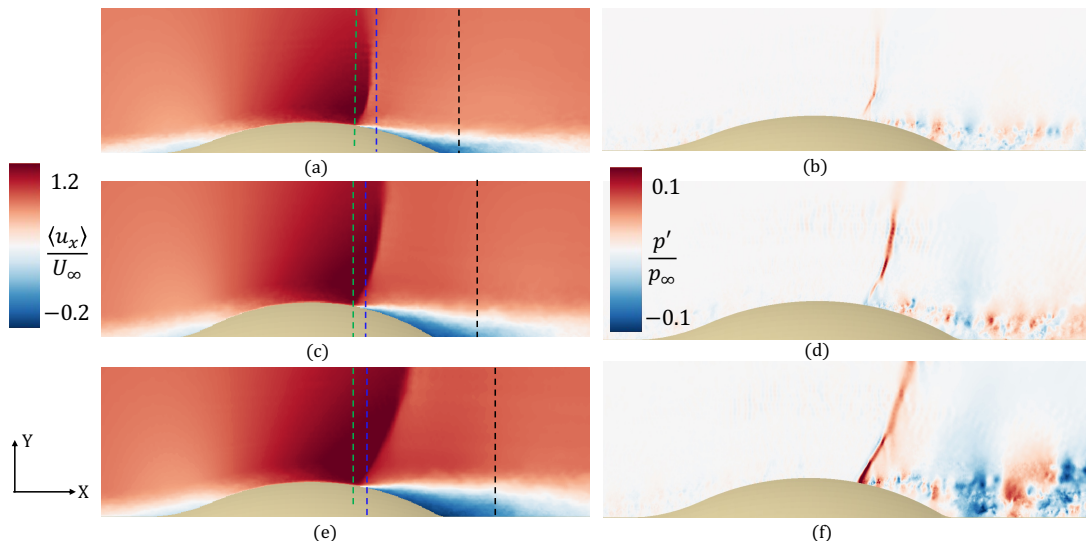


FIG. 12. Contours of time-averaged mean velocity (denoted as  $\langle u_x \rangle$ ) at (a)  $Ma_e = 0.85$ , (c)  $Ma_e = 0.875$  and (e)  $Ma_e = 0.90$  from wall modeled LES using the proposed wall model. The green, purple, and black dashed lines correspond to the location of the shock, the point of separation, and the point of reattachment, respectively. Subfigures (b), (d), and (f) present contours of the normalized, instantaneous pressure fluctuations ( $p'/p_\infty$ ) for flows at  $Ma_e = 0.85$ ,  $Ma_e = 0.875$  and  $Ma_e = 0.90$  respectively.

## VII. CONCLUDING REMARKS

In this work, a new wall model is proposed specifically aimed at identifying regions of strong near-wall flow non-equilibrium (in an averaged sense) that are inaccurately modeled using equilibrium boundary layer approximations. This region is presently ascertained in regions where the viscous pressure gradient velocity ( $u_p$ ) is significant compared to the friction velocity ( $u_\tau$ ). In these regions, the thin boundary layer equations used to approximate the wall stress are solved using the approximation of Kamogawa et al. [25] for the combined pressure gradient/convective terms. The performance of the proposed wall model is assessed on the flow over the Boeing Speed bump as a canonical case exhibiting smooth-body separation. Improvements in the grid-point scaling of the proposed model with Reynolds number compared to the equilibrium wall model are both hypothesized and then demonstrated in an *a posteriori* sense. The responsiveness of the model to adjust to small changes in freestream Mach number has been examined by performing wall-modeled LES of the transonic flow over the axisymmetric Bachalo-Johnson bump with the proposed model capturing the large differences in the  $C_p$  in the separation region (maximum difference between the extreme  $Ma_e$  cases being  $\Delta C_p \approx 0.25$ ) due to small changes in the Mach number (6% change). Overall, the results in this article demonstrate an improvement in the quantities of interest (such as the skin friction, surface pressure, and the mean velocity profiles) in boundary layers experiencing pressure gradients that lead to a smooth-body separation.

## ACKNOWLEDGEMENTS

This work was supported by NASA's Transformational Tools and Technologies project under grant number 80NSSC20M0201 and by Boeing Research & Technology. This research used resources from the Oak Ridge Leadership Computing Facility, which is a DOE Office of Science User Facility supported under Contract DE-AC05-00OR22725.



## APPENDIX I: CONNECTION BETWEEN THE VELOCITY-SCALE RATIO, $\frac{u_p}{u_\tau}$ , AND THE CRITICAL, VISCOUSLY STABLE INNER LAYER

Nickels [38] and Knopp et al. [67] argued that the relevant velocity scale in the near-wall region for a boundary layer experiencing pressure gradients is the local shear stress instead of the wall shear stress. Lozano-Durán and Bae [68] also corroborated this scaling for a turbulent channel flow with prescribed mean velocity profiles. Nickels [38] suggested that the critical value of the distance from the wall,  $y_c^+$  where the flow becomes viscously “unstable” and the effect of the pressure gradient becomes relevant is given by the relation,

$$\frac{|u_p^+|^3}{|u_\tau^+|^3} y_c^{+3} + y_c^{+2} - R_c^2 = 0 \quad (17)$$

where  $R_c \approx 12$  is the universal critical Reynolds number that determines the edge of the stable-viscous layer. For a zero pressure gradient boundary layer,  $y_c^+ \sim 12$ , coincides with the location of the peak production [69]. The height of the stable viscous layer will be significantly affected by the presence of pressure gradients if  $y_c^+ \frac{|u_p^+|^3}{|u_\tau^+|^3} = y_c^p \frac{|u_p^+|^2}{|u_\tau^+|^2} \sim 1$  or  $\frac{|u_p^+|}{|u_\tau^+|} \sim \sqrt{\frac{1}{y_c^p}} \sim \mathcal{O}(1)$ .

## APPENDIX II: SENSITIVITY OF PREDICTION OF FLOW SEPARATION TO SENSOR-ACTIVITY PARAMETER

In Equation 8, the ratio of  $\frac{|u_p^2|}{|u_\tau^2|}$  was bounded by the upper limit of  $\frac{\mathcal{O}(1)}{y_1^p[-A \log(y_1^p) + B]}$  for  $y_1^p \geq \mathcal{O}(10)$ , resulting in  $\frac{|u_p^2|}{|u_\tau^2|} \sim \mathcal{O}(1)$ . In this appendix, we test the sensitivity of the *a-posteriori* prediction of wall-modeled LES to the choice of this lower bound. Specifically, we consider the medium grid on the flow over the Boeing speed bump at  $Re_L = 2 \times 10^6$  (see Table I). Figure 13 shows that upon decreasing the threshold parameter ratio by an order of magnitude, the prediction of the pressure trace improves; as the flow approaches reattachment, the prediction of  $C_p$  is slightly better. Upon increasing the desired threshold ratio up to 10.0, the separation decreases significantly; the results are only slightly improved compared to the equilibrium wall model (which is the limit of the proposed model as the threshold ratio  $\frac{|u_p^2|}{|u_\tau^2|} \rightarrow \infty$ ). We also highlight that a threshold ratio larger than one is unphysical since, in that case,  $\mathcal{H}$  will exceed one. Secondly, in the vicinity of separation and reattachment points, this ratio is bound to reach infinitely large values eventually.

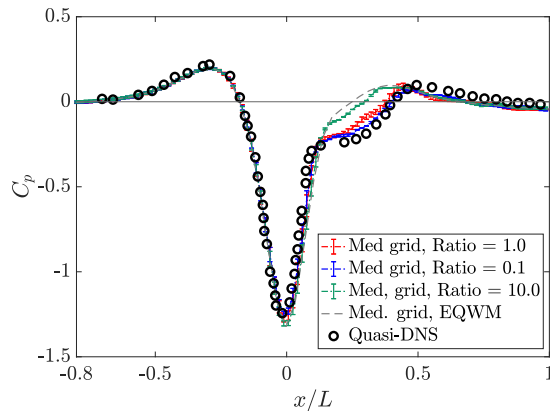


FIG. 13. Sensitivity of the streamwise surface pressure coefficient,  $C_p$  to the choice of the sensor activity parameter (ratio of  $|u_p|/|u_\tau|$ ). The flow considered here is that over the Boeing speed bump at  $Re_L = 2 \times 10^6$ . The reference quasi-DNS data is from Uzun and Malik [53].

## APPENDIX III: GRID CONVERGENCE FOR TRANSONIC BACHALO-JOHNSON BUMP FLOW

As remarked in Section VI B, our wall-modeled LES results for the flow over the Bachalo-Johnson bump at the lowest Mach number ( $Ma_e = 0.85$ ) slightly un-predict the flattening of the  $C_p$  curve in the separated region. In Figure 14(a), predictions from a more refined grid (2x refined homothetically compared to the 31 Mcv grid in Section VI B; refer to Table III for more details) are presented for both the equilibrium wall model and the proposed wall model. It is apparent that the proposed model improves the prediction of  $C_p$ , especially on the coarser grid. The prediction of the two models on the finer grid is more favorable with the experiments [60]. In Figure 14(b), the activity of the sensor is plotted across the two grids. On the finer grid, the sensor switches on slightly upstream in comparison to the coarser grid as the separation moves slightly upstream.

Mesh	$N_{cv}$	max $\Delta/c$	min $\Delta/c$	max. $\Delta/l_p$
Coarse	31 Mil.	$2.5 \times 10^{-1}$	$2 \times 10^{-3}$	$\approx 70$
Fine	120 Mil.	$2.5 \times 10^{-1}$	$1 \times 10^{-3}$	$\approx 35$

TABLE III. Mesh parameters for a  $60^\circ$  sector case of the transonic flow at  $Ma_e = 0.85$  over the bump in the experiments conducted by Bachalo and Johnson [60]. In the last column,  $l_p$  denotes the viscous length scale governed by the pressure gradient term,  $l_p = \nu/u_p$ .

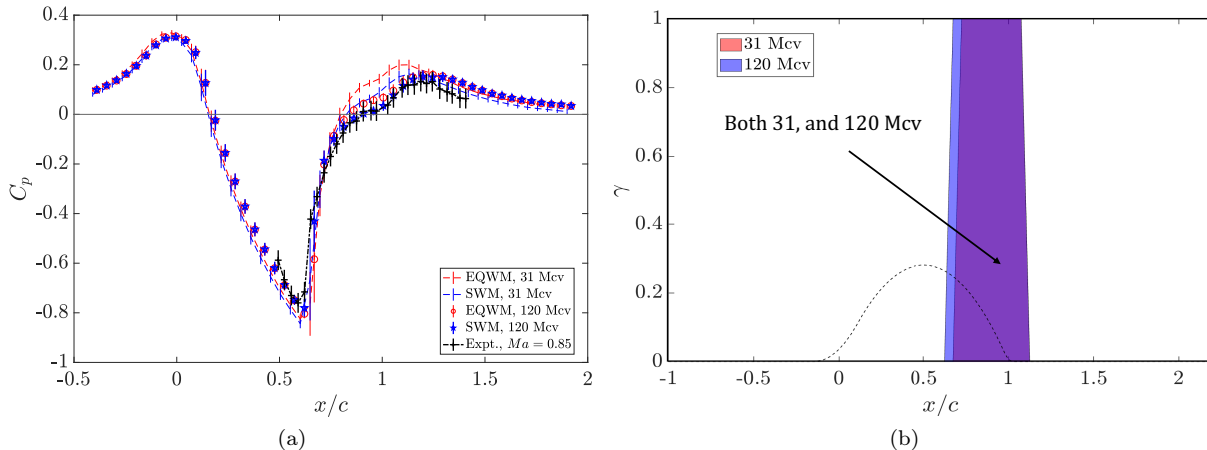


FIG. 14. Contours of time-averaged mean velocity (in the X direction, or at  $0^\circ$  azimuthal angle, denoted as  $\langle u_x \rangle$ ) from wall modeled LES (using 31 million control volumes) leveraging (a) the equilibrium wall model and (b) the proposed wall model.

- 
- [1] Stephen Pope. *Turbulent flows*. Cambridge university press, 2000.
  - [2] Joseph Smagorinsky. General circulation experiments with the primitive equations: I. the basic experiment. *Monthly Weather Review*, 91(3):99–164, 1963.
  - [3] Massimo Germano, Ugo Piomelli, Parviz Moin, and William H. Cabot. A dynamic subgrid-scale eddy viscosity model. *Physics of Fluids A: Fluid Dynamics*, 3:1760–1765, 1991.
  - [4] Franck Nicoud, Hubert Baya Toda, Olivier Cabrit, Sanjeeb Bose, and Jungil Lee. Using singular values to build a subgrid-scale model for large eddy simulations. *Physics of Fluids*, 23(8):085106, 2011.
  - [5] Bert Vreman, Bernard Geurts, and Hans Kuerten. On the formulation of the dynamic mixed subgrid-scale model. *Physics of Fluids*, 6(12):4057–4059, 1994.
  - [6] Wybe Rozema, Hyun J Bae, Parviz Moin, and Roel Verstappen. Minimum-dissipation models for large-eddy simulation. *Physics of Fluids*, 27(8):085107, 2015.
  - [7] Rahul Agrawal, Michael P. Whitmore, Kevin P. Griffin, Sanjeeb T. Bose, and Parviz Moin. Non-Boussinesq subgrid-scale model with dynamic tensorial coefficients. *Physical Review Fluids*, 7:074602, 2022-07.
  - [8] Xie Chenyue, Yuan Zelong, Wang Jianchun, et al. Artificial neural network-based subgrid-scale models for large-eddy simulation of turbulence. *Chinese Journal of Theoretical and Applied Mechanics*, 53(1):1–16, 2021.
  - [9] Zhideng Zhou, Guowei He, Shizhao Wang, and Guodong Jin. Subgrid-scale model for large-eddy simulation of isotropic turbulent flows using an artificial neural network. *Computers & Fluids*, 195:104319, 2019.
  - [10] H. Jane Bae, Adrián Lozano-Durán, Sanjeeb T. Bose, and Parviz Moin. Dynamic slip wall model for large-eddy simulation. *Journal of Fluid Mechanics*, 859:400–432, 2019. ISSN 14697645.
  - [11] XIA Yang, J Sadique, R Mittal, and Charles Meneveau. Integral wall model for large eddy simulations of wall-bounded turbulent flows. *Physics of Fluids*, 27(2):025112, 2015.
  - [12] Haechon Choi and Parviz Moin. Grid-point requirements for large eddy simulation: Chapman’s estimates revisited. *Physics of Fluids*, 24(1):011702, 2012.
  - [13] James W. Deardorff. A numerical study of three-dimensional turbulent channel flow at large Reynolds numbers. *Journal of Fluid Mechanics*, 41(2):453–480, 1970.
  - [14] William Cabot and Parviz Moin. Approximate wall boundary conditions in the large-eddy simulation of high Reynolds number flow. *Flow, Turbulence and Combustion*, 63(1):269–291, 2000.
  - [15] Konrad A. Goc, Oriol Lehmkuhl, George Ilhwan Park, Sanjeeb T. Bose, and Parviz Moin. Large eddy simulation of aircraft at affordable cost: a milestone in computational fluid dynamics. *Flow*, 1:E14, 2021.

- [16] Konrad A. Goc, Parviz Moin, Sanjeeb T. Bose, and Adam M. Clark. Wind tunnel and grid resolution effects in large-eddy simulations of the high-lift common research model. *Journal of Aircraft*, 0(0):1–13, 0.
- [17] Sanjeeb T. Bose and George Ilhwan Park. Wall-modeled large-eddy simulation for complex turbulent flows. *Annual Review of Fluid Mechanics*, 50:535–561, 2018.
- [18] Rahul Agrawal, Sanjeeb Bose, and Parviz Moin. Reynolds number dependence of length scales governing turbulent flow separation with application to wall-modeled large-eddy simulations. *arXiv preprint arXiv:2401.00075*, 2023.
- [19] Meng Wang and Parviz Moin. Dynamic wall modeling for large-eddy simulation of complex turbulent flows. *Physics of Fluids*, 14:2043–2051, 2002.
- [20] Elias Balaras, Carlo Benocci, and Ugo Piomelli. Two-layer approximate boundary conditions for large-eddy simulations. *AIAA Journal*, 34(6):1111–1119, 1996.
- [21] S Hickel, E Touber, J Bodart, and J Larsson. A parametrized non-equilibrium wall-model for large-eddy simulations. In *Proceedings of the Summer Program*, page 127. Citeseer, 2012.
- [22] George Ilhwan Park and Parviz Moin. An improved dynamic non-equilibrium wall-model for large eddy simulation. *Physics of Fluids*, 26(1):37–48, 2014.
- [23] George Ilhwan Park and Parviz Moin. Numerical aspects and implementation of a two-layer zonal wall model for les of compressible turbulent flows on unstructured meshes. *Journal of Computational Physics*, 305:589–603, 2016.
- [24] Jeffrey P Slotnick, Abdollah Khodadoust, Juan Alonso, David Darmofal, William Gropp, Elizabeth Lurie, and Dimitri J Mavriplis. Cfd vision 2030 study: a path to revolutionary computational aerosciences. Technical report, NASA/CR–2014-218178, 2014.
- [25] Ryo Kamogawa, Yoshiharu Tamaki, and Soshi Kawai. Ordinary-differential-equation-based nonequilibrium wall modeling for large-eddy simulation. *Physical Review Fluids*, 8(6):064605, 2023.
- [26] Y Na and Parviz Moin. Direct numerical simulation of a separated turbulent boundary layer. *Journal of Fluid Mechanics*, 374:379–405, 1998.
- [27] Konrad Goc, Sanjeeb T. Bose, and Parviz Moin. Subgrid-scale modeling sensitivities in wall-modeled large-eddy simulations of a high-lift aircraft configuration. *Center for Turbulence Research, Annual Research Briefs*, pages 49–58, 2020.
- [28] Konrad Goc, Sanjeeb Bose, and Parviz Moin. Wall-modeled large eddy simulation of an aircraft in landing configuration. In *AIAA Aviation 2020 Forum*, page 3002, June 2020.
- [29] Sanjeeb T. Bose and Parviz Moin. A dynamic slip boundary condition for wall-modeled large-eddy simulation. *Physics of Fluids*, 26(1):015104, 2014.
- [30] Michael P. Whitmore, Sanjeeb T Bose, and Parviz. Moin. Large-eddy simulation of a Gaussian bump with slip-wall boundary conditions. *Center for Turbulence Research, Annual Research Briefs*, pages 45–58, 2021.
- [31] Yuenong Ling, Gonzalo Arranz, Emily Williams, Konrad Goc, Kevin Griffin, and Adrián Lozano-Durán. Wall-modeled large-eddy simulation based on building-block flows. *arXiv preprint arXiv:2212.05120*, 2022.
- [32] Guillaume A. Brès, Sanjeeb T. Bose, Michael Emory, Frank E. Ham, Oliver T. Schmidt, Georgios Rigas, and Tim Colonius. Large-eddy simulations of co-annular turbulent jet using a Voronoi-based mesh generation framework. In *2018 AIAA/CEAS Aeroacoustics Conference*, page 3302, 2018.
- [33] Rahul Agrawal, Michael Whitmore, Konrad Goc, Sanjeeb T. Bose, and Parviz Moin. Reynolds number sensitivities in wall-modeled large-eddy simulation of a high-lift aircraft. *Center for Turbulence Research, Annual Research Briefs*, pages 229–244, 2023.
- [34] Hendrik Tennekes and John Leask Lumley. *A first course in turbulence*. MIT press, 1972.
- [35] Roger L Simpson. A model for the backflow mean velocity profile. *AIAA Journal*, 21(1):142–143, 1983.
- [36] BS Stratford. The prediction of separation of the turbulent boundary layer. *Journal of Fluid Mechanics*, 5(1):1–16, 1959.
- [37] Tie Wei, Yvan Maciel, and Joseph Klewicki. Integral analysis of boundary layer flows with pressure gradient. *Physical Review Fluids*, 2(9):092601, 2017.
- [38] TB Nickels. Inner scaling for wall-bounded flows subject to large pressure gradients. *Journal of Fluid Mechanics*, 521: 217–239, 2004.
- [39] K. P. Griffin, L. Fu, and P. Moin. Incorporating non-equilibrium effects in an ODE-based wall model. *Center for Turbulence Research, Annual Research Briefs*, pages 73–84, 2020.
- [40] H Jane Bae and Petros Koumoutsakos. Scientific multi-agent reinforcement learning for wall-models of turbulent flows. *Nature Communications*, 13(1):1443, 2022.
- [41] S Jovic and D Driver. Reynolds number effect on the skin friction in separated flows behind a backward-facing step. *Experiments in Fluids*, 18:464–467, 1995.
- [42] Eric W. Adams. *Experiments on the structure of turbulent reattaching flow*. Stanford University, 1984.
- [43] William J Devenport and E Peter Sutton. Near-wall behavior of separated and reattaching flows. *AIAA journal*, 29(1): 25–31, 1991.
- [44] Alexandra Bobke, Ricardo Vinuesa, Ramis Örlü, and Philipp Schlatter. History effects and near equilibrium in adverse-pressure-gradient turbulent boundary layers. *Journal of Fluid Mechanics*, 820:667–692, 2017.
- [45] Ricardo Vinuesa, Prabal Singh Negi, Marco Atzori, Ardeshir Hanifi, Dan S Henningson, and Philipp Schlatter. Turbulent boundary layers around wing sections up to  $Re_c = 1,000,000$ . *International Journal of Heat and Fluid Flow*, 72:86–99, 2018.
- [46] Álvaro Tanarro, Ricardo Vinuesa, and Philipp Schlatter. Effect of adverse pressure gradients on turbulent wing boundary layers. *Journal of Fluid Mechanics*, 883:A8, 2020.
- [47] O. Lehmkuhl, G. I. Park, S. T. Bose, and P. Moin. Large-eddy simulation of practical aeronautical flows at stall conditions. *Proceedings of the Summer Program 2018, Center for Turbulence Research, Stanford University*, pages 87–96, 2018.

- [48] Irwin Alber. Similar solutions for a family of separated turbulent boundary layers. In *9th Aerospace Sciences Meeting*, page 203, 1971.
- [49] Owen Williams, Madeline Samuell, E Sage Sarwas, Matthew Robbins, and Antonino Ferrante. Experimental study of a CFD validation test case for turbulent separated flows. In *AIAA Scitech 2020 Forum*, page 0092, 2020.
- [50] Patrick D Gray, Igal Gluzman, Flint Thomas, Thomas Corke, Matthew Lakebrink, and Kevin Mejia. A new validation experiment for smooth-body separation. In *AIAA Aviation 2021 Forum*, page 2810, 2021.
- [51] Patrick D. Gray, Igal Gluzman, Flint O. Thomas, and Thomas C. Corke. Experimental characterization of smooth body flow separation over wall-mounted Gaussian bump. In *AIAA Scitech 2022 Forum*, page 1209, 2022.
- [52] Patrick D. Gray, Igal Gluzman, Flint O. Thomas, Thomas C. Corke, Matthew T. Lakebrink, and Kevin Mejia. Benchmark characterization of separated flow over smooth Gaussian bump. In *AIAA Aviation 2022 Forum*, page 3342. AIAA, 2022-06. ISBN 978-1-62410-635-4. doi:10.2514/6.2022-3342.
- [53] Ali Uzun and Mujeeb R. Malik. High-fidelity simulation of turbulent flow past Gaussian bump. *AIAA Journal*, 60(4):2130–2149, 2022.
- [54] Di Zhou and H Jane Bae. Sensitivity analysis of wall-modeled large-eddy simulation for separated turbulent flow. *preprint, arXiv:2309.13555*, 2023.
- [55] Gonzalo Arranz, Yuenong Ling, and Adrian Lozano-Duran. Wall-modeled les based on building-block flows: Application to the gaussian bump. In *AIAA Aviation 2023 Forum*, page 3984, 2023.
- [56] Rahul Agrawal, Sanjeeb T. Bose, and Parviz Moin. Wall modeled LES of the Boeing speed bump using a non-Boussinesq modeling framework. *Center for Turbulence Research, Annual Research Briefs*, pages 43–58, 2022.
- [57] Rahul Agrawal, Sanjeeb T. Bose, Kevin P. Griffin, and Parviz Moin. An extension of Thwaites method for turbulent boundary layers. *preprint, arXiv:2310.16337*, 2023.
- [58] Di Zhou, Michael P Whitmore, Kevin P Griffin, and Hyunji Jane Bae. Large-eddy simulation of flow over boeing gaussian bump using multi-agent reinforcement learning wall model. In *AIAA Aviation 2023 Forum*, page 3985, 2023.
- [59] Frank M White. *Fluid mechanics*. The McGraw Hill Companies, 2008.
- [60] WD Bachalo and DA Johnson. Transonic, turbulent boundary-layer separation generated on an axisymmetric flow model. *AIAA Journal*, 24(3):437–443, 1986.
- [61] Kyle P Lynch, Blake W Lance, Nathan E Miller, Matthew F Barone, and Steven J Beresh. Experimental characterization of an axisymmetric transonic separated flow for computational fluid dynamics validation. *AIAA Journal*, 61(4):1623–1638, 2023.
- [62] Dennis C Jespersen, Thomas H Pulliam, and Marissa Lynn Childs. Overflow turbulence modeling resource validation results. Technical report, NASA, NAS-2016-01, 2016.
- [63] Philippe R Spalart, Kirill V Belyaev, Andrey V Garbaruk, Mikhail L Shur, Mikhail Kh Strelets, and Andrey K Travin. Large-eddy and direct numerical simulations of the bachalo-johnson flow with shock-induced separation. *Flow, Turbulence and Combustion*, 99(3-4):865–885, 2017.
- [64] Yu Lv, Xiang IA Yang, George I Park, and Matthias Ihme. A discontinuous galerkin method for wall-modeled large-eddy simulations. *Computers & Fluids*, 222:104933, 2021.
- [65] CC Horstman and DA Johnson. Prediction of transonic separated flows. *AIAA journal*, 22(7):1001–1003, 1984.
- [66] DM Schatzman and FO Thomas. An experimental investigation of an unsteady adverse pressure gradient turbulent boundary layer: embedded shear layer scaling. *Journal of Fluid Mechanics*, 815:592–642, 2017.
- [67] Tobias Knopp, Nico Reuther, Matteo Novara, Daniel Schanz, Erich Schüle, Andreas Schröder, and CJ Kähler. Experimental analysis of the log law at adverse pressure gradient. *Journal of Fluid Mechanics*, 918:A17, 2021.
- [68] Adrián Lozano-Durán and Hyunji Jane Bae. Characteristic scales of Townsend’s wall-attached eddies. *Journal of Fluid Mechanics*, 868:698–725, 2019.
- [69] John Kim, Parviz Moin, and Robert Moser. Turbulence statistics in fully developed channel flow at low Reynolds number. *Journal of Fluid Mechanics*, 177:133–166, 1987.